Fluid Dynamics
Research

PAPER • **OPEN ACCESS**

Large eddy simulation of the variable density mixing layer

To cite this article: J X Huang *et al* 2021 *Fluid Dyn. Res.* **53** 015507

OPEN ACCESS
IOP Publishing | The Japan Society of Fluid Mechanics Fluid Dynamics Research
Fluid Dyn. Res. **53** (2021) 015507 (28pp) https://doi.org/10.1088/1873-7005/abdb3f

Large eddy simulation of the variable density mixing layer

J X Huang, S N Hug and W A McMullan

School of Engineering, University of Leicester, University Road, Leicester LE1 7RH,
United Kingdom

E-mail: andrew.mcmullan@le.ac.uk

Received 25 September 2020; revised 14 December 2020
Accepted for publication 13 January 2021
Published 10 February 2021

Communicated by Professor Graham Owen Hughes

Abstract

In this paper we perform large eddy simulations of variable density mixing layers, which originate from initially laminar conditions. The aim of this work is to capture the salient flow physics present in the laboratory flow. This is achieved through varying the nature of the inflow condition, and assessing the vortex structure present in the flow. Two distinct inflow condition types are studied; the first is an idealised case obtained from a mean inflow velocity profile with superimposed pseudo-white-noise, and the second is obtained from an inflow generation technique. The inflow conditions generated have matching mean and root mean squared statistics. Validation of the simulations is achieved through grid dependency and subgrid-scale model testing. Regardless of the inflow condition type used, the change in growth rate of the mixing layer caused by the density ratio is captured. It is found that the spacing of the large-scale spanwise structure is a function of the density ratio of the flow. Detailed interrogation of the simulations shows that the streamwise vortex structure present in the mixing layer depends on the nature of the imposed inflow condition. Where white-noise fluctuations provide the inflow disturbances, a spatially-stationary streamwise structure is absent. Where the inflow generator is used, a spatially stationary streamwise structure is present, which appears as streaks in plan-view visualisations. The stationary streamwise structure evolves such that the ratio of streamwise structure wavelength to local vorticity thickness asymptotes to unity, independent of the density ratio. This value is in agreement with previous experimental studies. Recommendations are made on the requirements of inflow condition modelling for accurate mixing layer simulations.

Keywords: mixing layers, coherent structures, streamwise vortices

(Some figures may appear in colour only in the online journal)

1. Introduction

The variable density free shear layer is important in a number of practical engineering applications, including combustion and aeroacoustics. The simplest type of free shear layer is the plane turbulent mixing layer, which forms through the merging of two parallel streams of fluid of differing velocities and densities. The mixing layer has been studied for 80 years, and it has been the subject of extensive research owing to the discovery of quasi-two-dimensional coherent structures embedded within the turbulent flow at high Reynolds numbers (Brown and Roshko 1974). Substantial research effort has been expended into elucidating the dynamics of the structures (Dimotakis and Brown 1976, Hernan and Jimenez 1982, Browand and Troutt 1985), and the effects of the structures on entrainment and mixing in the layer (Koochesfahani and Dimotakis 1986, Karasso and Mungal 1996, Pickett and Ghandhi 2002, Meyer *et al* 2006). The structures have been observed across the range of Reynolds numbers (Winant and Browand 1974) and Mach numbers (Papamoschou and Roshko 1988), reported experimentally, and they are present in flows where large density variations occur owing to the composition of the freestreams (Bernal and Roshko 1986), or through exothermic heat release within the mixing layer (Mungal and Dimotakis 1984, Hermanson and Dimotakis 1989).

After almost 50 years of research into coherent structures in plane turbulent mixing layers, a clear picture of their evolution has remained elusive. Studies of the flow at low Reynolds number showed that mixing layer growth occurred in a stepwise fashion owing to the interaction between primary spanwise vortices, with phase jitter causing a mean overall linear growth (Winant and Browand 1974). At higher Reynolds number, experimental evidence for this stepwise growth is lacking; analysis of cine-film visualisations have shown that the majority of the growth of the mixing layer occurs between interactions at high Reynolds number (Hernan and Jimenez 1982). Theoretical arguments show that this continuous growth should have a square-root-of-time dependency through either turbulent diffusion (Moore and Saffman 1975), or irrotational roll-up (Jimenez 1980), with interactions between structures permitting the overall mean linear growth of the layer. More recent experiments, however, have shown that the growth of the structures can be continuous and linear, with interactions between the structures contributing nothing to the overall growth of the flow (D'Ovidio and Coats 2013). Doubt also remains as to the ubiquity of the coherent structure for all initial conditions (Chandrsuda *et al* 1978), as the structures are not so readily apparent in shear layers originating from turbulent boundary layers (Slessor *et al* 1998). The quasi-two-dimensional structure is observed in experiments where the upstream flow is laminar, with a low-level background fluctuation environment (Brown and Roshko 2012) —conditions that are typically referred to as 'clean' initial conditions (Bell and Mehta 1992).

A vortex structure orientated parallel to the streamwise direction can also exist in the mixing layer. In flow visualisation the streamwise vortex structure appeared as 'streaks' (Konrad 1976), and it was subsequently found that the streamwise vortices are, in a mean sense, statistically stationary (Bernal and Roshko 1986, Bell and Mehta 1992, Plesniak *et al* 1993, Wiecek and Mehta 1998). The streamwise vortices originate from residual streamwise vorticity in the laminar boundary layers upstream of the mixing layer (Bell and Mehta 1992), with the spacing of the vortices increasing with streamwise distance. Experimental evidence suggests that the scaling of the wavelength of the streamwise structure to the local vorticity thickness will asymptote to approximately unity (Jimenez 1983, Bernal and Roshko 1986, Bell and Mehta 1992), but it is not currently clear if this ratio is valid for all values of density ratio and velocity ratio. The ubiquity of the streamwise structure for all initial conditions remains an open research question (Bell and Mehta 1990).

Subsonic variable-density mixing layer experiments are normally performed with helium comprising the low-density gas, and with either nitrogen or air as the constituent high-density gas. The use of bottled helium results in experimental run-times of a few seconds, which means that the initial conditions of variable-density mixing layers are poorly-documented. For numerical simulation methods such as direct numerical simulation (DNS), and large eddy simulation (LES), the lack of inflow condition information renders direct replication of experiments very difficult (in numerical simulation the term ‘inflow condition’ has the same meaning as initial conditions in experiments). Temporal mixing layer DNS and LES studies have shown that the imposed initial conditions can substantially affect both the mean flow statistics, and the internal geometry of the coherent structures (Comte *et al* 1992, Rogers and Moser 1994, Balaras *et al* 2001). In spatially-developing mixing layer simulations, the specification of the inflow condition is a significant challenge. For initially-laminar mixing layers, many studies simplify the inflow condition by imposing a mean velocity profile onto which Gaussian white noise is added at each time step (Comte *et al* 1998, Attili and Bisetti 2012, McMullan *et al* 2015). These idealised inflow conditions produce reasonable mean flow statistics for uniform density mixing layers when compared to experiment (Attili and Bisetti 2012, McMullan *et al* 2015), but the stationary streamwise structure is not present in the simulated flow (Comte *et al* 1998, McMullan and Garrett 2016b). Recent research has shown that employing an inflow generation technique provides the residual streamwise vorticity in the upstream conditions which is necessary to generate the stationary streamwise structure (McMullan and Garrett 2016a, McMullan 2017).

There are very few published studies concerning the numerical simulation of the variable-density turbulent mixing layer. Most studies consider the temporally-evolving flow (Almagro *et al* 2017, Baltzer and Livescu 2020), and the spatially-developing flow is usually confined to two-dimensional boxes for reasons of computational cost (Soteriou and Ghoniem 1995). Confining the flow to a two-dimensional box necessarily prevents the development of the streamwise vortex structure, and restricts the mixing layer to growth through pairings interactions between spanwise vortices (McMullan 2018a). A LES study of the variable density mixing layer on a three-dimensional computational domain has shown that the dependency of the mixing layer growth on the density ratio can be captured (McMullan *et al* 2011). To date, no published simulation has been able to capture both the spanwise-orientated, and streamwise-orientated, vortex structures that are present in variable-density mixing layers originating from clean laminar conditions.

In this research we simulate the isothermal mixing layer at varying values of the density ratio. This research generalises the simulations of McMullan and Garrett (2016a), where only uniform density mixing layers were considered. The aim of this research is to capture the salient flow features present in variable-density mixing layers which originate from ‘clean’ inflow conditions. The simulated mixing layers originate from laminar conditions, with a low-level fluctuation environment representative of the initial conditions present in laboratory-scale wind tunnels. Two different forms of inflow condition are utilised, which develop inflow data that have matching mean velocity profiles, and root mean squared velocity fluctuation profiles. The effects of the nature of the inflow condition on the predicted mixing layer are assessed over a range of density ratios, at a fixed velocity ratio. Particular attention is paid to the large-scale, spanwise-orientated, turbulent vortex structures, and the streamwise vortex structure. This paper is organised as follows: Numerical methods are outlined in section 2. Details of the reference experiment, and the set-up of the numerical simulations, is outlined in section 3. Validation of the computational mesh, and the influence of subgrid-scale modelling, are detailed in section 4. Main simulation results are presented in section 5, and conclusions are drawn in section 6.

2. Numerical methods

Using Einstein's summation convention, the continuity equation, species mass transport equation, momentum equation, energy equation, and equation of state are for a reacting compressible flow are given by

$$\frac{\partial \rho}{\partial t}+\frac{\partial \rho u_i}{\partial x_i}=0, \tag{1}$$

$$\frac{\partial \rho Y_k}{\partial t}+\frac{\partial \rho (u_i+V_{k,i})Y_k}{\partial x_i}=\dot{\omega}_k \text{ for } k=1,2,\ldots,N, \tag{2}$$

$$\frac{\partial \rho u_i}{\partial t}+\frac{\partial \rho u_i u_j}{\partial x_j}=-\frac{\partial p}{\partial x_i}+\frac{\partial \tau_{ij}}{\partial x_j}+\rho\sum_{k=1}^{N} Y_k f_{k,i}, \tag{3}$$

$$\frac{\partial \rho h}{\partial t}+\frac{\partial \rho u_i h}{\partial x_i}=\frac{Dp}{Dt}-\frac{\partial q_i}{\partial x_i}+\tau_{ij}\frac{\partial u_i}{\partial x_j}+\dot{Q}+\rho\sum_{k=1}^{N} Y_k f_{k,i}\dot{V}_k, \tag{4}$$

$$p=\rho\sum_{k=1}^{N}\frac{Y_k}{M_k}R_u T \tag{5}$$

where ρ is the density, u_i is the velocity, N is the total number of species, Y_k is the mass fraction of species k, V_k is the diffusion velocity of species k, p is the pressure, τ_{ij} is the viscous stress tensor, h is the enthalpy per unit mass, q_i is the heat flux in the i direction, $\dot{Q}$ is the rate of heat increase in the system, $\dot{\omega}_k$ is the rate of mass production of species k, M_k is the molecular weight of species k, R_u is the universal gas constant, f is a body force, and T is the temperature. The current research focuses on the LES of incompressible, isothermal, low-speed variable density mixing layers, which permits a number of simplifying assumptions to be made to the governing equations. It is assumed that Fick's Law of diffusion is valid for the current flows, and that the Lewis number is unity. It is assumed that the mixing layers studied here are sufficiently low-speed that compressibility effects are not important, which permits the use of the low-Mach number approximation. The pressure and density fields are therefore decoupled, removing acoustic effects from the flow. Body forces are also ignored in the current research. Non-reacting two-stream flows at isothermal conditions can be represented by a single scalar variable, commonly-referred to as the mixture fraction.

Under the previous assumptions, applying an implicit top-hat filter to the governing equations lead to the filtered low-Mach number equations of continuity, momentum, and mixture fraction transport. These are written as

$$\frac{\partial \bar{\rho}}{\partial t}+\frac{\partial \bar{\rho}\tilde{u}_i}{\partial x_i}=0, \tag{6}$$

$$\frac{\partial \bar{\rho}\tilde{u}_i}{\partial t} + \frac{\partial \bar{\rho}\tilde{u}_i\tilde{u}_j}{\partial x_j} = -\frac{\partial \bar{p}}{\partial x_i} + \frac{\partial \tau_{ij}}{\partial x_j} - \frac{\partial T_{ij}}{\partial x_j}, \tag{7}$$

$$\frac{\partial \bar{\rho}\tilde{\xi}}{\partial t} + \frac{\partial \bar{\rho}\tilde{u}_i\tilde{\xi}}{\partial x_i} = \frac{\partial J_i}{\partial x_i} - \frac{\partial M_i}{\partial x_i}, \tag{8}$$

respectively, where a quantity $\overline{\phi}$ denotes a spatially-filtered variable, and $\tilde{\phi}$ denotes a Favre-filtered variable. For a Newtonian fluid obeying Fick's law of diffusion, the mass flux is given by $J_i = \gamma(\partial\tilde{\xi}/\partial x_i)$, where $\gamma = \bar{\rho}\Gamma$ denotes the mass diffusivity coefficient. The filtering operation introduces extra terms into the governing equations which must be modelled to close the system. The subgrid stress and mass flux tensors are given by $T_{ij} = \overline{\rho}(\widetilde{u_i u_j} - \tilde{u}_i\tilde{u}_j)$ and $M_i = \overline{\rho}(\widetilde{u_i\xi} - \tilde{u}_i\tilde{\xi})$.

A subgrid-scale model is used to close the governing equations. The standard Smagorinsky model (Smagorinsky 1963), and the WALE model (Nicoud and Ducros 1999), are used to model the subgrid-stresses. In the Smagorinsky model, the subgrid viscosity is computed using

$$\mu_{\text{sgs}} = \bar{\rho}(C_s\Delta)^2|\tilde{S}_{ij}|, \tag{9}$$

where Δ is the filter width, and the magnitude of the strain-rate tensor is given by $|\tilde{S}_{ij}| = \sqrt{2\tilde{S}_{ij}\tilde{S}_{ij}}$, with $\tilde{S}_{ij} = \frac{1}{2}(\partial\tilde{u}_i/\partial x_j + \partial\tilde{u}_j/\partial x_i)$. The Smagorinsky model is widely-used, but its limitations are well understood. The model coefficient, C_s, is not universal, requiring modification for individual flow configurations. The model predicts finite subgrid-scale viscosity in regions of laminar flow, and it also displays incorrect near-wall behaviour. The near-wall deficiency is usually corrected through a van Driest damping function (Van Driest 1956), which drives the subgrid viscosity to zero at the wall. In the WALE model the subgrid viscosity is computed through

$$\mu_{\text{sgs}} = \bar{\rho}(C_w\overline{\Delta})^2\frac{(S^d_{ij}S^d_{ij})^{3/2}}{(\overline{S}_{ij}\overline{S}_{ij})^{5/2} + (S^d_{ij}S^d_{ij})^{5/4}}, \tag{10}$$

where $S^d_{ij} = \frac{1}{2}(\overline{g}^2_{ij} + \overline{g}^2_{ji} - \frac{1}{3}\delta_{ij}\overline{g}^2_{kk})$, $\overline{g}^2_{ij} = \overline{g}_{ik}\overline{g}_{kj}$, and $\overline{g}_{ij} = \partial\overline{u}_i/\partial x_j$. This model overcomes many of the deficiencies of the Smagorinsky model, in that the correct near-wall behaviour is captured, and zero subgrid viscosity is produced in regions of laminar flow. These features make the model attractive for shear layer simulations where the flow originates from laminar upstream conditions.

The mixture fraction transport equation is closed with the commonly-used gradient-diffusion model, given by

$$M_i = -\frac{\mu_{\text{sgs}}}{Sc_t}\left(\frac{\partial\tilde{\xi}}{\partial x_i}\right). \tag{11}$$

In this study the subgrid-scale Schmidt number is assumed constant, and takes a value of $Sc_t = 0.7$. For the isothermal variable density flows considered here the density field is related to the mixture fraction variable through

$$\frac{1}{\bar{\rho}} = \frac{\tilde{\xi}}{\rho_1} + \frac{1-\tilde{\xi}}{\rho_2}, \tag{12}$$

where ρ_1 and ρ_2 are the freestream densities of the high- and low-speed streams respectively.

The governing equations of motion are solved using a finite volume method with a staggered cell arrangement. A second-order accurate central differencing scheme is used to evaluate terms in the momentum equation. A third-order accurate total variation diminishing (TVD) scheme is used for the convective and diffusive terms in the scalar transport equation. The TVD scheme is used for the scalar transport in order to minimise out of bounds errors in the solution of the equation (Dianat *et al* 2006). The outflow condition is a standard convective condition similar to that used in previous uniform density studies of the mixing layer flow (McMullan *et al* 2007). The second order accurate Adams–Bashforth method is used to temporally advance the governing equations. The pressure field is computed using a multi-grid method.

Two distinct methods of generating the simulation inflow condition are used in this study. The first is obtained by imposing a mean streamwise velocity profile at the inflow plane, onto which Gaussian pseudo-white noise is superimposed at each time step. This inflow technique produces spectral information that is very similar to other studies in which this method is utilised (Attili and Bisetti 2012, McMullan *et al* 2015), with the spectral energy of the fluctuations being several orders of magnitude lower than that present in the most unstable frequency of the flow. The second method employed is the inflow condition generator of Xiao *et al* (2017). This method is similar to other recycling methods (Lund *et al* 1998) where small domains are placed upstream of the main simulation domain, in which the inflow condition is generated. The flow in the virtual domain is recycled in order to produce a time-dependent inflow condition, and the flow in the virtual domain is rescaled at specified intervals, to match a target set of statistics. The flow field that passes through the downstream end of the virtual domain is then fed into the main mixing layer domain to provide the inflow condition.

3. Simulation set–up

3.1. Reference experiment

For this study it was decided that a uniform-density mixing layer experiment with well-documented initial conditions would provide reference data for validation purposes, and the effects of density ratio on the flow could then be assessed against the uniform density results.

The experiments of Browand and Latigo (1979) provide the reference data. These uniform-density experiments were performed with a high-speed stream velocity, $U_1 = 25.6\ \mathrm{ms}^{-1}$, and a low-speed stream velocity, $U_2 = 5.2\ \mathrm{ms}^{-1}$. The upstream boundary layers were laminar, and close to Blasius form. The high-speed side boundary layer momentum thickness was measured as $\theta_1 = 0.457$ mm, and the low-speed stream momentum thickness was $\theta_2 = 0.86$ mm. In the high-speed side boundary layer a peak streamwise velocity root mean squared (r.m.s.) fluctuation magnitude of $u'/U_1 \approx 2.5\%$, was recorded. The fluctuation measurement was, however, subject to a 1% measurement error and are therefore were somewhat unreliable. No information on the vertical velocity fluctuation, v', or the spanwise velocity fluctuation, w', was recorded. These flow conditions can be considered as clean, laminar upstream flow. The velocity ratio parameter, R, defined as

$$R = \frac{U_1 - U_2}{U_1 + U_2}, \tag{13}$$

was calculated at the trailing edge of the splitter plate as $R = 0.66$. The density ratio, s, defined as

$$s = \frac{\rho_2}{\rho_1}, \tag{14}$$

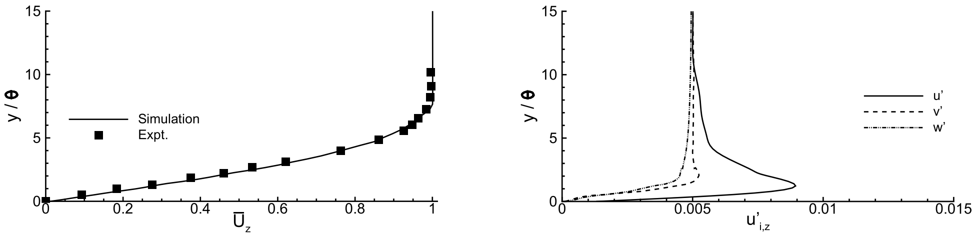

(a) Mean streamwise velocity.

(b) Streamwise velocity r.m.s. fluctuation.

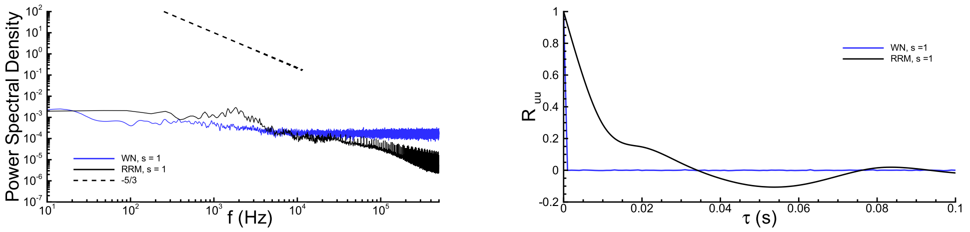

(c) Streamwise velocity fluctuation power spectral density at $x = 0$.

(d) Autocorrelation of streamwise velocity fluctuation at $x = 0$.

Figure 1. Boundary layer flow statistics at the trailing edge of the splitter plate, $x/\theta_i = 0$. Normalised flow statistics are identical for each freestream. Subscript z denotes a spanwise-averaged quantity.

was unity for the experimental mixing layer with air as the constituent gas of both freestreams. Extensive measurements on the growth of the mixing layer, and its mean velocity statistics, were reported. Subsequent experiments in the same facility investigated the spatially-stationary streamwise vortex structure present in the mixing layer (Huang and Ho 1990).

3.2. Simulation parameters

For the flow conditions described in section 3.1, simulations are performed with $s = 0.138$, 1.0, and 7.23. The uniform density simulations match the bulk experimental flow conditions, with the other simulations designed to test the effects of extreme density ratio on the flow. It is assumed that the boundary layer mean streamwise velocity profiles do not vary as a function of the density of the freestream fluid. Two distinct inflow condition types are assessed in this study. The first is obtained through imposing mean velocity profiles at the inflow plane of the mixing layer domain, onto which pseudo-random Gaussian white noise is superimposed at each time step. Simulations with this inflow type are denoted ‘WN’. The second type of inflow condition is obtained from recycling and rescaling method, and are denoted ‘RRM’. Mean and r.m.s. flow statistics gathered at the inflow plane to the mixing layer domain in both simulation types are shown in figures 1(a) and (b). Although the profiles are identical for both simulation types, there will be differences in the spectral content owing to the nature of the applied inflow condition. Figure 1(c) shows the power spectral density (PSD) of the streamwise velocity fluctuation at the inflow plane, in the vicinity of the splitter plate. These data are obtained from calculations at $s = 1$. The WN case has a fairly flat spectrum across the entire frequency range, as would be expected for pseudo-random-number perturbations. The RRM case has a similar spectrum, but with an accumulation of energy at $f \approx 1050$ Hz. The autocorrelations of the same velocity signals are shown in figure 1(d). The WN velocity signal

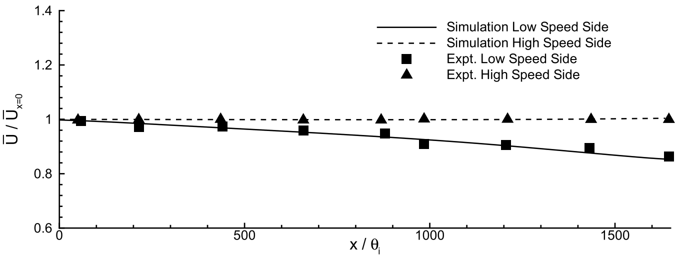

Figure 2. Variation of freestream velocity with downstream distance in a uniform density mixing layer simulation. Freestream velocity values are recorded at a vertical distance of $y/\theta_i = 328$ from the horizontal plane of the splitter plate in both streams.

Table 1. Properties of the mixing layer domain meshes used for simulation validation.

Grid	Cells ($N_x \times N_y \times N_z$)	$\Delta x_{\min}/\theta_i$	$\Delta y_{\min}/\theta_i$	$\Delta z/\theta_i$
Grid 1	$768 \times 256 \times 256$	0.44	0.0875	1.54
Grid 2	$480 \times 224 \times 224$	0.875	0.175	1.76

rapidly drops to zero correlation, which is again expected for pseudo-random numbers. In the RRM case, the recycling method produces a velocity field with a temporal correlation—in this simulation the integral time scale is $\tau_0 \approx 0.005$ s.

The computational domain in which the mixing layer is simulated extends $1630 \times 1326 \times 392\theta_i$ in the streamwise (x), vertical (y), and spanwise (z) directions respectively, where θ_i is the initial momentum thickness of the mixing layer. It has been shown that the initial momentum thickness is equivalent to the high-speed side boundary layer momentum thickness, θ_1 (Browand and Latigo 1979). The vertical extent of the domain matches that of the experimental test section, in order to mimic the pressure gradient present in the experimental facility. Figure 2 shows the freestream velocity variation of a typical uniform-density mixing layer calculation in the computational domain. The evolution of both freestream velocities with streamwise distance accurately replicates the data from the experiment. The virtual domains required for the RRM method contain $256 \times 128 \times 256$ cells, and extend $112 \times 663 \times 392\theta_i$ upstream of the main mixing layer domain. For the RRM-type calculations the splitter plate is modelled as a no-slip boundary with infinitesimal thickness. This assumption is justifiable as the splitter plate tip does not significantly affect the flow if its thickness is less than 50% of the total displacement thickness of the departing boundary layers (Dziomba and Fiedler 1985) — a condition which is satisfied here.

Grid dependence studies are performed through using two different meshes. The properties of the meshes are detailed in table 1. Grid 1 represents the main production grid in this study, and Grid 2 is a coarse mesh used for comparison. Stretching of the mesh is employed on both grids to improve the grid resolution in regions of steep velocity gradients near the plane of the splitter plate, and to reduce the cell count in regions of low flow variability. On both grids the minimum streamwise grid spacing is applied in the region $0 \leq x/\theta_i \leq 22$ in order to resolve the primary instability in the flow. Beyond $x/\theta_i = 22$, a constant grid expansion factor of 1.003 is applied to Grid 1, and a factor if 1.01 is applied to Grid 2. In the vertical direction, and expansion factor of 1.04 is applied on Grid 1, and a factor of 1.05 is applied to Grid 2. On Grid 1, 36 points resolve the high-speed side boundary layer velocity profile, whilst on Grid 2 there are 28 grid points within the boundary layer thickness. Grid 1 has been used elsewhere to simulate the uniform density mixing layer, with excellent results obtained (McMullan and Garrett 2016a, 2016b, McMullan 2017). On Grid 1 the effect of subgrid scale modelling is assessed by performing simulations with the Smagorinsky model at a coefficient value $C_s = 0.1, 0.18$, and with the WALE model at a coefficient value of $C_w = 0.3, 0.56$.

On both grids the upper and lower walls of the domain are modelled as slip walls. The spanwise boundaries are periodic, and the spanwise domain extent is sufficiently large that the flow is not artificially confined by the periodicity (McMullan 2015, 2018b). The outflow condition is of a standard convective form. The non-dimensional time step is $\Delta t/(\theta_i/U_1) = 0.033$ for the $s = 1.0, 7.23$ calculations, and $\Delta t/(\theta_i/U_1) = 0.022$ for the $s = 0.138$ cases. The simulations are run until a statistically stationary flow-field is established, after which statistical samples are collated over a period corresponding to the time required for a fluid parcel to travel through the computational domain ten times at the low-speed stream velocity. During the run flow visualisation data are sampled at a rate of 1.67 kHz. The run-time over which statistics are accumulated is of the same order as the duration of variable-density mixing layer experiments. For the statistical sampling period, the variation in spanwise-averaged second-order statistical quantities is less than 0.5% over a period of one flow-through time.

The simulations here produce mixing layers with a maximum local Reynolds number of $\mathrm{Re}_\delta = \Delta U \delta_{viz}/\nu_2 = 315{,}000$, where ΔU is the velocity difference across the layer, δ_{viz} is the local visual thickness, and ν_2 is the kinematic viscosity of the low-speed stream (Bernal and Roshko 1986). All of the mixing layers simulated here attain Reynolds numbers well beyond the $\mathrm{Re}_\delta \approx 10^4$ required for the mixing transition to occur (Dimotakis 2000).

4. Subgrid–scale model and grid resolution validation

Grid resolution tests, and subgrid-scale model validation studies, have been performed for all density ratios. The trends observed are very similar for each density ratio (Huang *et al* 2017), hence for the sake of brevity and clarity, all of the simulations presented in the validation section have been performed at uniform density conditions to permit comparison with the reference experimental data. The WN-type inflow condition is used for all simulations in this section.

4.1. Grid validation

The momentum thickness of the mixing layer can be computed from

$$\theta = \frac{1}{\rho_1 \Delta U^2} \int_{-\infty}^{\infty} \overline{\rho}(U_1 - \overline{U})(\overline{U} - U_2)\mathrm{d}y, \tag{15}$$

where $\overline{U}$ is the mean streamwise velocity. The momentum thickness distributions shown in figure 3(a) have good agreement with the experimental data on both grids. The linear slope in the momentum thickness curves indicates that the flow has become self-similar, and the gradient of this slope compares well with experimental data. The mean streamwise velocity profiles recorded at $x/\theta_i = 1000$ are shown in figure 3(b). Excellent agreement is obtained between the experiment and both simulations. The streamwise r.m.s. fluctuation profiles at $x/\theta_i = 1000$, presented in figure 3(c), show that Grid 1 produces better comparison with the reference data than Grid 2, particularly towards the outer edges of the mixing layer. Finally the streamwise evolution of the peak magnitude of the streamwise r.m.s. fluctuation is shown in figure 3(d). The over-estimation of the overshoot in u' at $x/\theta_i \approx 250$ is common in simulations originating from WN-type inflow conditions (McMullan *et al* 2015, McMullan and Garrett 2016a). Similarly the streamwise location of this overshoot is predicted further downstream in WN-type

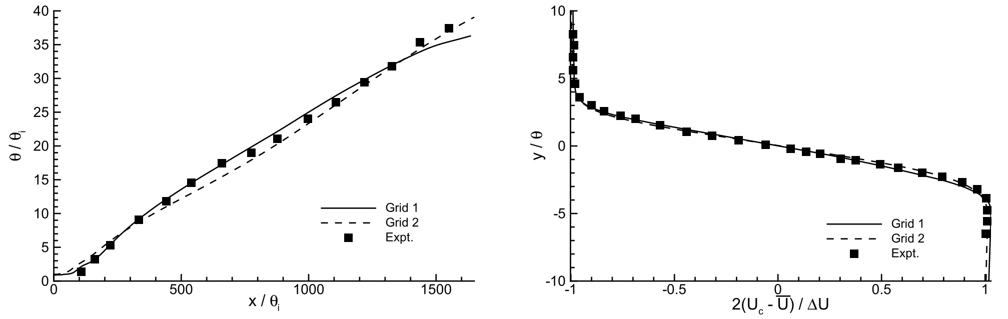

(a) Momentum thickness.

(b) Mean streamwise velocity at $x/\theta_i = 1000$.

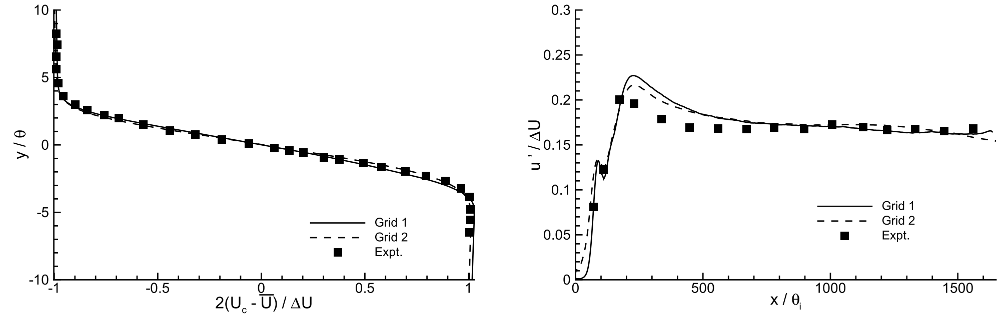

(c) Streamwise velocity r.m.s. fluctuation at $x/\theta_i = 1000$.

(d) Maximum Streamwise r.m.s. fluctuation evolution.

Figure 3. Flow statistics gathered in the grid resolution study. Reference experimental data obtained from Browand and Latigo (1979). All simulations shown in this figure originate from WN-type inflow conditions at a density ratio $s = 1$.

calculations than in experiments (McMullan *et al* 2015). Both simulations do, however, predict an asymptotic value of u' that agrees well with the experiment. Based on these results, Grid 1 was chosen to simulate the remainder of the cases in this study.

4.2. Subgrid–scale model tests

The effect of the subgrid-scale model on the flow predicted with Grid 1 is now assessed. Four simulations are performed; Smagorinsky model cases with $C_s = 0.1$, 0.18, and WALE model cases with $C_w = 0.3$, 0.56. Figure 4 shows contour maps of the high-speed stream concentration, ζ, and contour lines of the ratio of subgrid viscosity to molecular viscosity, at an arbitrary time instant in each simulations. The initial region of the mixing layer is shown, where the flow is laminar. The effect of the Smagorinsky model coefficient can be seen in figures 4(a) and (b); increasing the value of C_s introduces elevated subgrid viscosity into the region of laminar flow. In contrast, an increase in the WALE model coefficient (figures 4(c) and (d)) does not introduce additional viscosity into the laminar region.

The flow statistics shown in figure 5 provide more quantitative information on the effects of the subgrid-scale model on the simulated flow. The momentum thickness distributions in

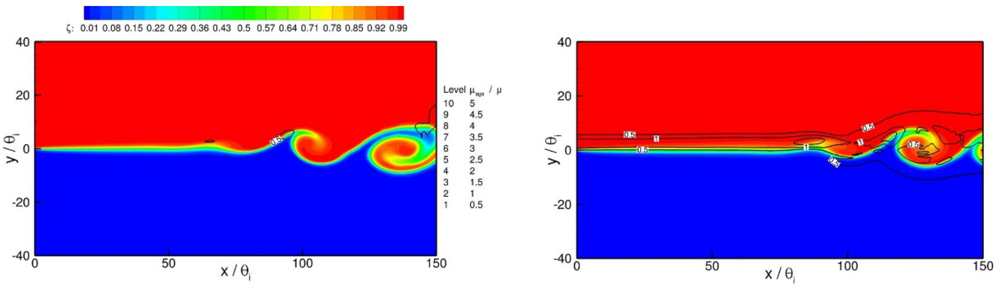

(a) Smagorinsky model, $C_s = 0.1$.

(b) Smagorinsky model, $C_s = 0.18$.

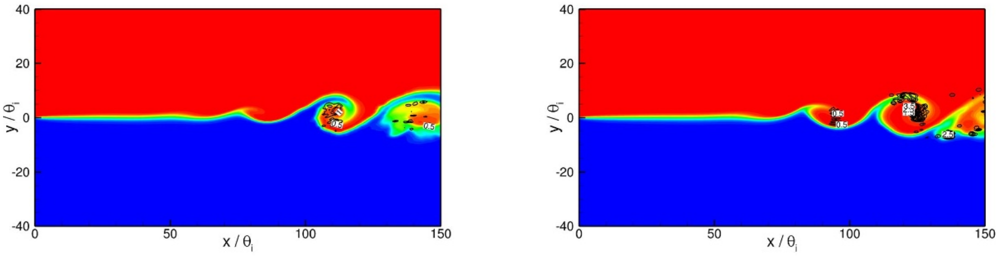

(c) WALE model, $C_w = 0.3$.

(d) WALE model, $C_w = 0.56$.

Figure 4. Contour maps of highs-speed stream concentration, and contour lines of the ratio of subgrid viscosity to molecular viscosity, μ_{sgs}/μ, at an arbitrary time step. Only the initial region of the flow, where the shear layer is laminar, is shown for clarity. All simulations shown in this figure originate from WN-type inflow conditions on Grid 1, with $s = 1$.

figure 5(a) show that the initial evolution of the mixing layer is delayed in the $C_s = 0.18$ case in the region $0 < x/\theta_i < 450$, whereas the initial evolution of the other cases agree better with the experimental data. The mean streamwise velocity profiles, and rms streamwise velocity fluctuation profiles, obtained at $x/\theta_i = 1000$ are shown in figures 5(b) and (c) respectively. These profiles agree well with the reference data, and they are largely unaffected by the subgrid-scale modelling. The evolution of the maximum streamwise rms velocity fluctuation is shown in figure 5(d). The curve from the $C_s = 0.18$ simulation shows a substantial delay in the evolution of u' when compared to the other cases, and there is a poor comparison with the reference data in the region of $x/\theta_i < 700$. The asymptotic values of u' attained in the self-similar region of all simulations compare well with the experimental data.

The Smagorinsky model introduces additional viscosity into the simulated flow, which delays the development of the mixing layer towards a self-similar state. High values of C_s produce elevated levels of additional viscosity, which exacerbate the delay in flow evolution. As the WALE model predicts vanishing values of subgrid viscosity in the laminar region, the predicted flow is insensitive to the choice of C_w. Once a self-similar state has been attained, however, all of the simulations shown here achieve the same self-similar state. Minimising the dependency of the flow evolution on the choice of subgrid-scale model is essential, particularly flow mixing layers originating from laminar upstream conditions. For this reason the WALE model with a coefficient value $C_w = 0.56$ is chosen to for all further calculations.

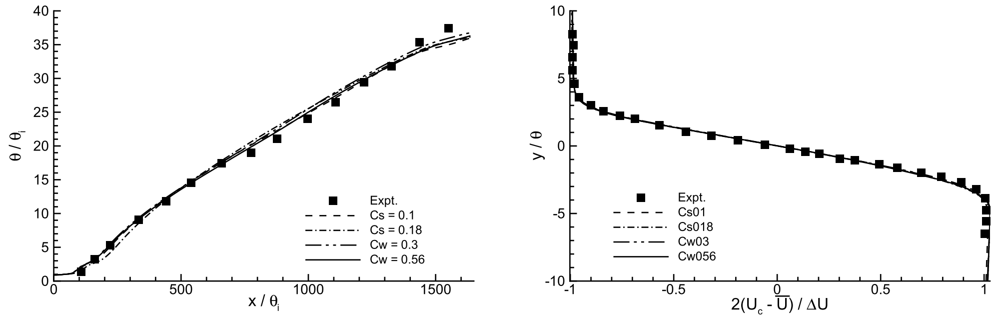

(a) Momentum thickness.

(b) Mean streamwise velocity at $x/\theta_i = 1000$.

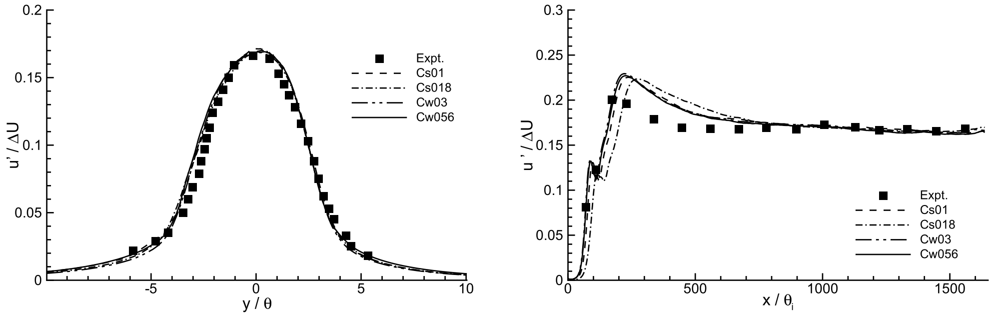

(c) Streamwise velocity r.m.s. fluctuation at $x/\theta_i = 1000$.

(d) Maximum Streamwise r.m.s. fluctuation evolution.

Figure 5. Flow statistics gathered in the subgrid-scale model dependency study. Reference experimental data obtained from Browand and Latigo (1979). All simulations shown in this figure originate from WN-type inflow conditions on Grid 1, with $s = 1$.

5. Variable density mixing layer simulations

For the flow conditions described in section 3.1, simulations are performed at density ratios of $s = 0.138$, 1.0, and 7.23 on Grid 1. The effect of the inflow condition on the simulated mixing layer is assessed by running a WN-type and a RRM-type simulation for each density ratio.

5.1. Flow statistics

The momentum thickness for each simulation is shown in figure 6(a). The effect of the density ratio on the mixing layer development can clearly be seen in the profiles; an increasing value of s leads to an increase in the growth of the mixing layer. There is an increase of a factor of approximately ten in the momentum thickness of the mixing layer between the extremes of the density ratio. The profiles show a region of linear growth in the momentum thickness, indicating that all simulations have reached a self-similar turbulent state. At uniform-density conditions, both inflow condition types produce mixing layer with momentum thickness distributions that agree well with the experimental data. The predicted curves, however, do not collapse onto each other—this implies that there are differences in the computed flow field, as a result of the change in imposed inflow condition. The low density ratio simulations ($s = 0.138$) produce momentum thickness curves which are reasonably closely matched to each

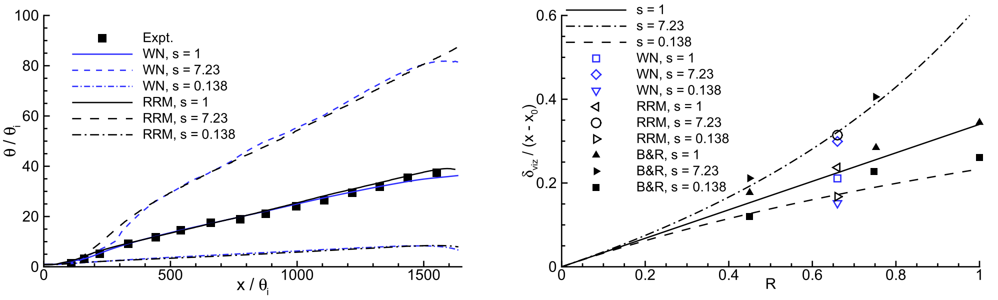

(a) Momentum thickness variation.

(b) Visual thickness growth rates.Experimental data (B&R) from Brown & Roshko (1974).

Figure 6. Measures of the mixing layer growth obtained from simulations on Grid 1 for varying density ratios. The visual thickness is obtained from the 1% thickness of the mixing layer.

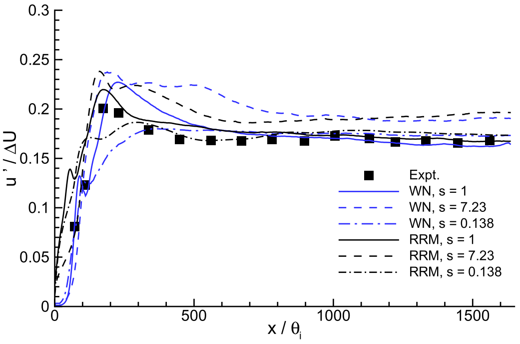

Figure 7. Peak values of streamwise r.m.s. velocity fluctuation as a function of streamwise distance.

other, although some differences are apparent. At the high density ratio ($s = 7.23$), differences between the momentum thickness plots are more noticeable. The approach to a linear slope in the momentum thickness is substantially delayed in the WN-type simulation, when compared to its RRM-type counterpart.

A more commonly-used measure of variable-density mixing layer growth is the visual thickness. This quantity is obtained from the vertical distance between the mean high-speed concentration levels, $\overline{\zeta} = 0.01, 0.99$. Here the measurement is recorded at $x/\theta_i = 1500$. The visual thickness growth rate is defined as $\delta'_{\mathrm{viz}} = \delta_{\mathrm{viz}}/(x - x_0)$, where x_0 is the virtual origin of the flow. The virtual origin is computed from the streamwise location at which the $\overline{\zeta} = 0.01, 0.99$ concentration lines intersect. The visual thickness growth rate of each simulation is shown in figure 6(b). Included in this graph are the experimental data of Brown and Roshko (1974), and the predictions of a mixing layer growth model (Dimotakis 1986). The simulations yield visual thickness growth rates that are in the range of the experimental data, and that are in good agreement with the growth model. It is important to note, however, that the WN-type calculations produce a growth rate that is up to 11% lower than their RRM-type counterparts. This discrepancy between the growth rates provides further evidence that there is a change in the flow dynamics between the simulation types.

Figure 7 shows the evolution of the maximum value of u' as a function of streamwise distance. The uniform-density RRM-type simulation produces very good agreement with the

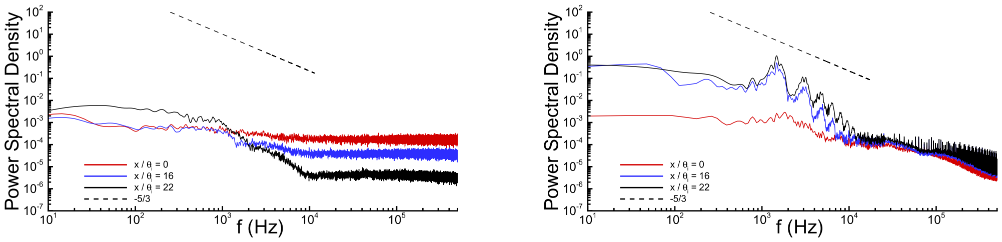

(a) WN, $s = 1$.

(b) RRM, $s = 1$.

Figure 8. Evolution of the streamwise velocity fluctuation spectra in the initial region of the mixing layer. Data obtained from uniform-density simulations.

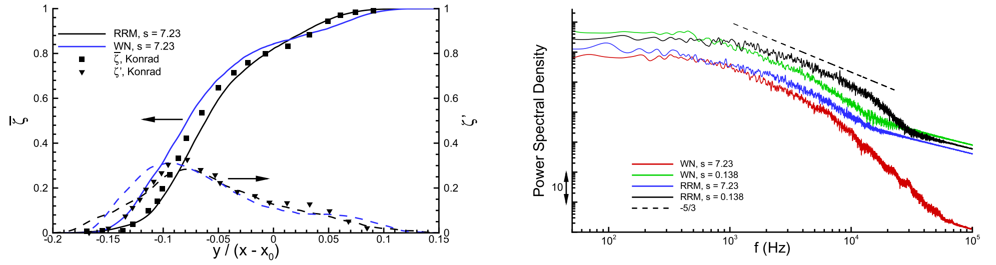

(a) Mean concentration, and rms concentration fluctuation at $x/\theta_i = 1000$.

(b) Concentration fluctuation spectra at $x/\theta_i = 328$.

Figure 9. Statistical information on the high-speed concentration in the simulations. Experimental data recorded in (a) recorded with $R = 0.45$, and a local Reynolds number of $\mathrm{Re}_\delta = 40\,000$ (Konrad 1976). Reynolds number of WN-type case is $\mathrm{Re}_\delta = 177\,000$, and $\mathrm{Re}_\delta = 184\,000$ for the RRM-type case.

reference data, and the overshoot of u' is predicted at the correct streamwise location. The maximum overshoot in the WN-type uniform-density calculation is predicted further downstream than the reference experiment; this feature is common in simulations which originate from this form of inflow condition (McMullan *et al* 2015). For a given inflow condition type both the evolution of u', and its asymptotic value, are functions of the density ratio. For all density ratios the WN-type simulations require a longer streamwise distance in order to attain an asymptotic value of u', when compared to the RRM-type calculations.

The evolution of the flow in the initial region of the mixing layer is investigated through PSD plots of the streamwise velocity fluctuation, as shown in figure 8 for the $s = 1$ cases. For the WN simulations (figure 8(a)), the high-frequency fluctuations decay rapidly with increasing streamwise distance from the inflow plane, and there is no clear dominant frequency in the spectrum at $x/\theta_i = 22$. For the RRM case, a clear dominant frequency in the spectrum develops immediately downstream of the inflow plane to the main mixing layer domain. The peak frequency of $f \approx 1440$ Hz is in reasonable agreement with the prediction of linear stability theory for the present flow conditions (Monkewitz and Huerre 1982). The delayed development of a dominant instability mode in the WN simulation is the cause of the delayed evolution of the mixing layers that originate from these conditions.

Figure 9(a) shows the concentration statistics at $x/\theta_i = 1000$ for the $s = 7.23$ simulations, along with the experimental data of Konrad (1976). In figure 9(a) the vertical co-ordinate is normalised by the streamwise distance from the virtual origin, $(x - x_0)$, for consistency with the experimental data. It should be noted that these experimental data were recorded for a mixing layer with $R = 0.45$, at a local Reynolds number of $\mathrm{Re}_\delta = 40\,000$. The local Reynolds numbers of the WN and RRM simulations are 177 000 and 184 000 respectively, hence the comparison in figure 9(a) is meant for guidance purposes only. The mean and r.m.s. concentration profiles obtained in both $s = 7.23$ simulations compare favourably with the experimental data. The inflection point in the mean profile on the high-speed side is more pronounced in the WN-type simulation.

PSD plots of the concentration fluctuation are shown in figure 9(b) for the variable density cases. These spectra were recorded on the geometric plane of the splitter plate ($y/\theta_i = 0$) at the streamwise location $x/\theta_i = 328$. The curves have been shifted along the vertical axis for clarity. All four spectra display a $-5/3$ roll-off indicative of turbulent flow. The transition to turbulence in the mixing layer is precipitated by pairing interactions between primary vortices, in agreement with previous experimental studies (Huang and Ho 1990). The uniform density calculations also show turbulent behaviour at this streamwise location (McMullan and Garrett 2016a).

The flow statistics presented here show that both simulation types produce favourable comparisons with experiment, and that the effect of the density ratio is captured in the simulations. Some discrepancies in the flow statistics between the simulation types are notable, and the causes of these discrepancies are explored below.

5.2. Vortex structure

The simulated flow is visualised through a numerical analogue of schlieren imagery, where the gradient of the density field is used to visualise the flow (Quirk 1997). The visualisations are averaged along the line of sight of the image to maintain consistency with the experimental technique used to discover coherent structures in turbulent mixing layers (Brown and Roshko 1974).

Typical instantaneous visualisations from the $s = 7.23, 0.138$ calculations using the WN inflow condition are shown in figure 10. The plan view is shown in the upper part of the image, and the side view is shown in the lower part. For the $s = 7.23$ case large spanwise-orientated vortex structures are clearly visible in the side view. Following the roll-up of the flow, the laminar spanwise vortices undergo a transition to turbulence; in figure 10(a) the transition occurs at $x/\theta_i \approx 330$ with a pairing interaction between spanwise rollers. Large variations in the streamwise position of the transition are observed, owing to the variability in the locations at which the triggering interactions occur. In the plan view of figure 10(a) the primary vortices are parallel to the span, and a secondary structure forms on the spanwise rollers once the first pairing of vortices has taken place. There is no evidence for a secondary structure forming as a result of the roll-up of the mixing layer into primary vortices—a phenomenon noted in experiments of the high density ratio mixing layer (Bernal and Roshko 1986). A typical flow visualisation of the WN-type, $s = 0.138$ simulation is shown in figure 10(b). The side view also shows laminar vortices immediately downstream of the inflow plane, which also undergo a transition to turbulence through the mechanism described above. The turbulent vortex structure is present in the side view, but it somewhat difficult to ascertain; the structures are most easily discerned through the presence of thick interconnecting braids between the structures. The plan view shows that the laminar vortices are not aligned parallel with the span, and that the vortices undergo localised pairings prior to the transition to turbulence—these localised pairing are clearly visible at $x/\theta_i = 120$, $z/\theta_i \approx 300$ in the plan view of figure 10(b). Localised

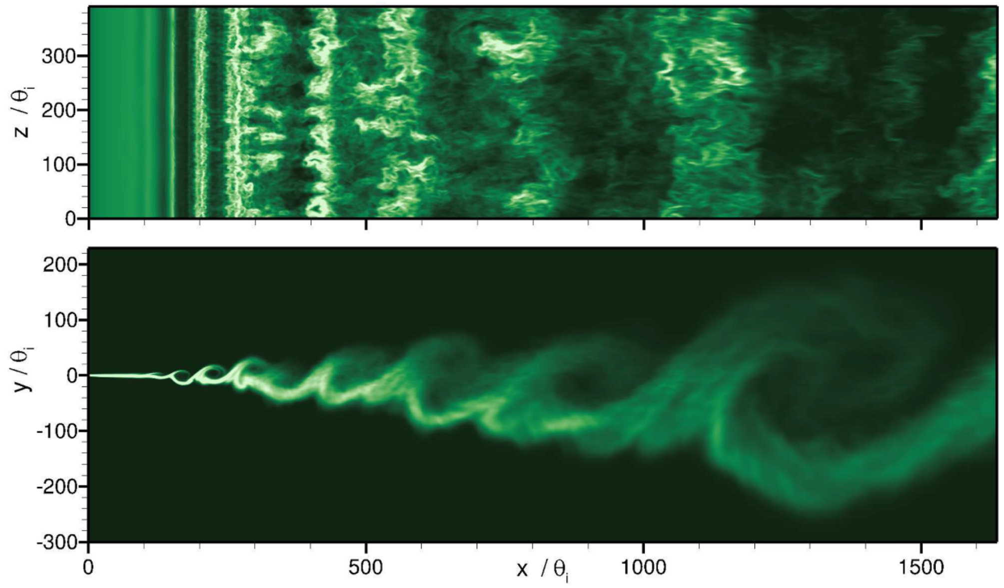

(a) $s = 7.23$.

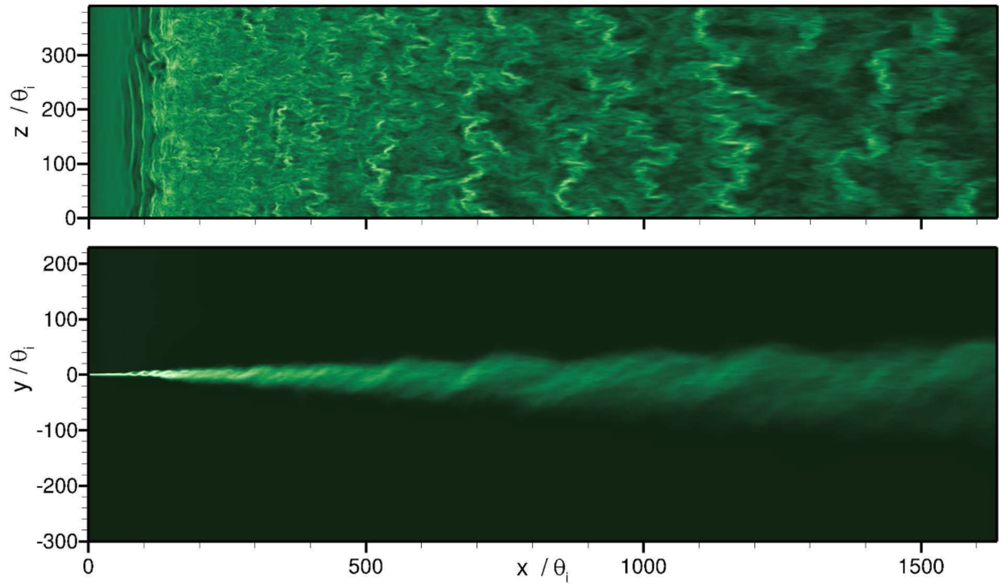

(b) $s = 0.138$.

Figure 10. Numerical schlieren images obtained at an arbitrary instant in time from variable-density mixing layer simulations with WN-type inflow conditions. Upper part of image is the plan view, lower part of image is the side view.

pairings interactions between laminar vortices are common in uniform-density mixing layer simulations that originate from WN-type inflow conditions (Comte *et al* 1992, Comte *et al* 1998, McMullan and Garrett 2016a).

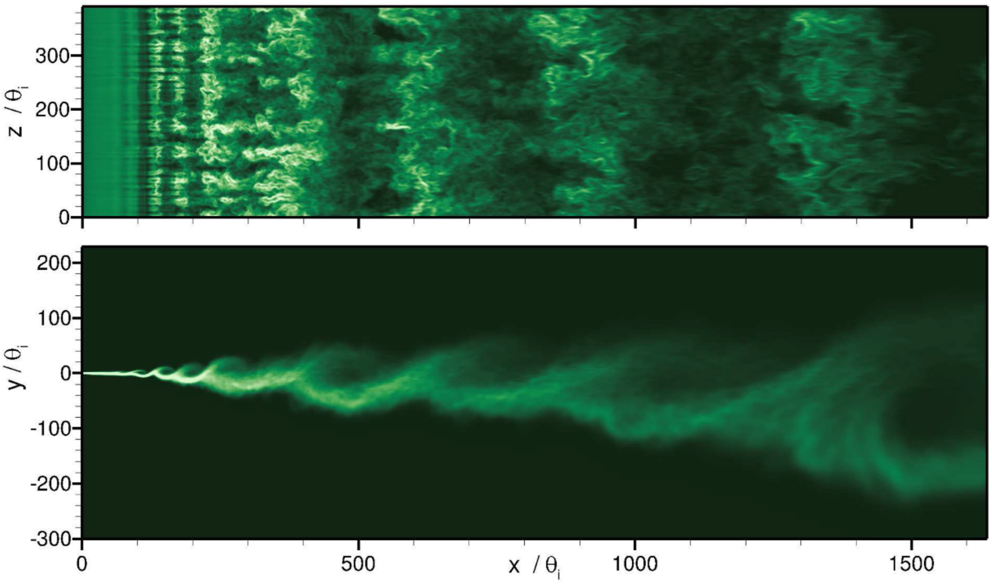

(a) $s = 7.23$.

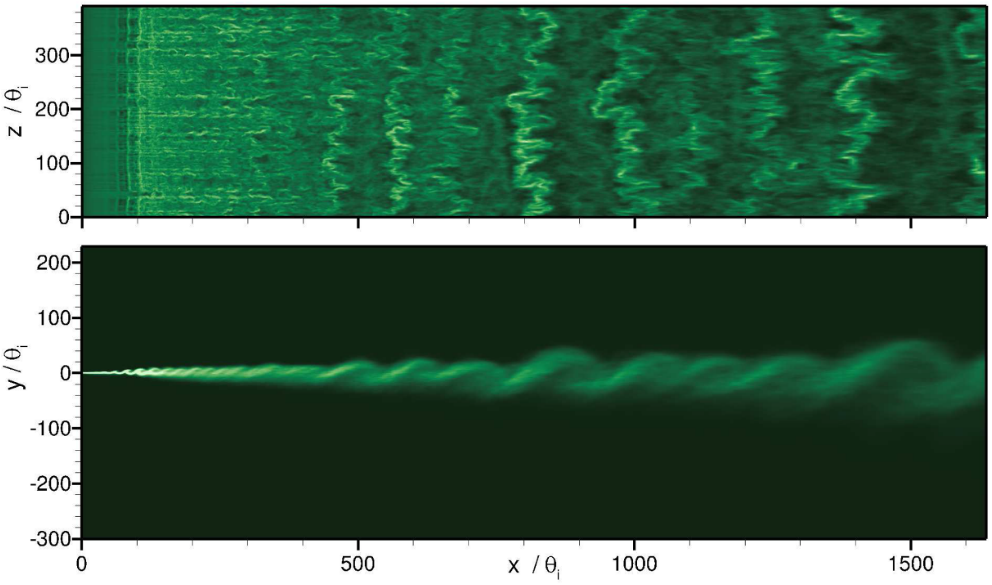

(b) $s = 0.138$.

Figure 11. Numerical schlieren images obtained at an arbitrary instant in time from variable-density mixing layer simulations with RRM-type inflow conditions. Upper part of image is the plan view, lower part of image is the side view.

Visualisations of the $s = 7.23, 0.138$ mixing layers using the RRM inflow condition are shown in figure 11. The side-view visualisation of the $s = 7.23$ case shows that large vortex structures are visible throughout the streamwise extent of the domain, and the laminar vortices undergo a transition to turbulence through pairing interactions. The plan-view visualisation in figure 11(a) shows that a streaky structure is present in the flow; this streaky structure is organised parallel to the streamwise direction, with the streaks spaced at regular intervals across the span. The streaky structure develops downstream of $x/\theta_i \approx 80$ in the image, coinciding with the roll-up of the flow into primary Kelvin–Helmholtz (K–H) vortices. The streaky structure is particularly notable in the laminar region, and it also extends into the turbulent region where it becomes less well-defined. The plan-view flow visualisation of the $s = 0.138$ case in figure 11(b) shows that a streaky structure is also present in the mixing layer. As with the $s = 7.23$ simulation, the streaks develop with the emergence of K–H vortices in the side-view image. The large-scale turbulent vortex structures in the side-view image are much more obvious in this simulation when compared to the WN-type simulation of the same density ratio (figure 10(b)).

The flow visualisation images shown here can be qualitatively compared with the experimental images of the seminal Caltech experiments (Brown and Roshko 1974, Konrad 1976, Bernal and Roshko 1986). The RRM-type simulations capture both the large-scale spanwise-orientated turbulent structures which persist in the turbulent region, and also the streaky structure which is orientated in the streamwise direction. The images presented in figure 11 bear remarkable resemblance to the visualisations of Konrad (1976), and suggests that these simulations capture the salient flow features present in the laboratory flow. Although the WN-type simulations capture a large-scale spanwise-orientated structure, the streaky structure is not present in the visualisations. Quantitative analysis of the vortex structures present in the simulations is outlined below.

5.2.1. Spanwise structure. In each simulation up to 1800 snapshots of flow visualisation images, along with the associated velocity field, and concentration field, are recorded. The flow-fields are analysed to produce topographical information on the spanwise-orientated vortex structures present in the each simulation.

A typical turbulent vortex structure is shown in figure 12(a). This particular structure was captured in the RRM-type simulation at $s = 7.23$. Figure 12(a) shows a contour map of the normalised spanwise-averaged streamwise velocity $\tilde{u}_z/U_1$, along with contour lines of the spanwise-averaged concentration field, ζ_z. The structure core is visible at $x/\theta_i \approx 910$, and it has a roughly circular cross-section. Through the vertical plane of the structure core there is a local acceleration of the freestream velocity towards the upper edge of the structure, and there is a local deceleration of the freestream velocity towards the lower edge of the structure. The local accelerations and decelerations are caused by a concentration of spanwise vorticity inducing motion in its vicinity, and they are a reliable indicator of the passage of spanwise-orientated turbulent vortex structures. This phenomenon has also been observed in mixing layer experiments (Browand and Troutt 1980, Browand and Troutt 1985).

Numerical probes are placed near the outer edges of the mixing layer ($y/\theta_i = \pm 90$) at a streamwise position of $x/\theta_i = 656$, and at mid-span of the computational domain. The streamwise velocity at both probe locations is recorded for the entire duration of the simulation. A short section of the velocity signals are shown in figure 12(b). The peaks in the high-speed stream trace align with the valleys in the low-speed stream signal, indicating the passage of turbulent vortex structures through the sampling plane. A total of 14 structures pass through the probe streamwise location during the sample shown in figure 12(b).

For all stored flow snapshots, the local accelerations are tracked for each structure throughout its lifetime. A vertical line which intersects the streamwise position of maximum local

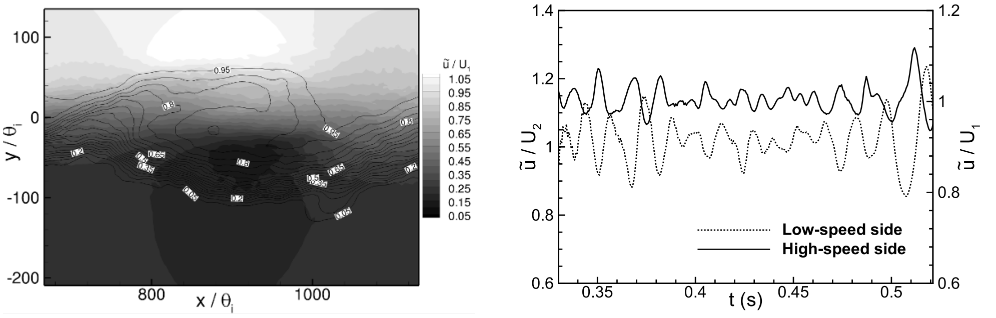

(a) Contour map of normalised streamwise velocity, $\tilde{u}_z/U_1$, and contour lines of spanwise-averaged high-speed concentration, ζ_z.

(b) Velocity traces recorded at $y/\theta_i = \pm 90$ at the streamwise location $x/\theta_i = 656$.

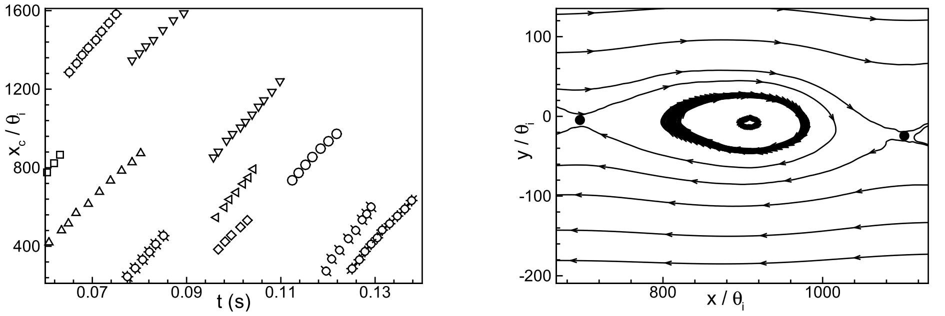

(c) Convection tracks of the cores of several structures.

(d) Instantaneous streamlines in the Lagrangian frame. Filled circles denote locations of saddle points.

Figure 12. Spanwise turbulent vortex structure features in the RRM-type simulation with $s = 7.23$. Structure features are typical of all recorded structures for this density ratio.

acceleration/deceleration defines the streamwise location of the structure core. Tracks of structure cores are shown in figure 12(c) for an arbitrary sample of the simulation, taken from the RRM, $s = 7.23$ case. The tracks show the convection of structures from their birth up to the point where they interact with a neighbour. Each structure convects at a roughly constant speed throughout its lifetime. The convection velocity is a weak function of streamwise distance from the splitter plate owing to the effect of the adverse pressure gradient on the freestream velocities, as shown in figure 1. The mean convection velocity is computed from the average convection speed of all structures captured—with up to 200 individual structures forming the sample in each simulation. The mean structure convection velocities are listed in table 2. It can be seen that the mean convection velocity is a function of the density ratio, closely matching the relationships

$$U_c = \frac{U_1 + U_2}{2}(1 + \Lambda R) \tag{16}$$

where Λ is the density ratio parameter, $\Lambda = (\sqrt{\rho_1} - \sqrt{\rho_2})(\sqrt{\rho_1} + \sqrt{\rho_2})$. The convection velocity of the flow is biased towards the more-dense stream, such that the heavy fluid 'drags'

Table 2. Statistical information on the large-scale spanwise structures present in the simulated mixing layer.

Inflow type	s	U_c (ms^{-1})	$l/(x - x_0)$
WN	0.138	20.02	0.22
WN	1	15.16	0.33
WN	7.23	10.8	0.45
RRM	0.138	20.06	0.241
RRM	1	15.22	0.36
RRM	7.23	10.79	0.474

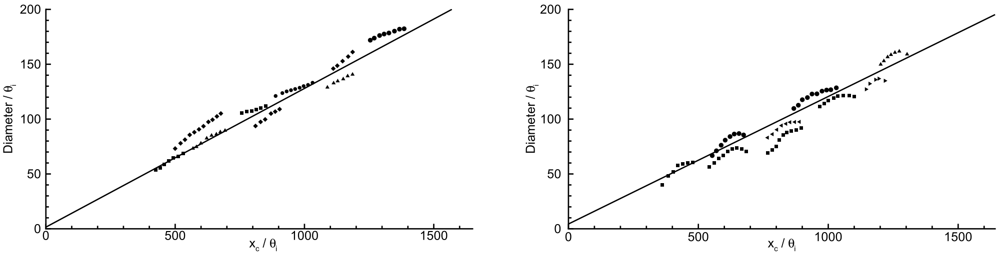

(a) WN, $s = 0.138$. (b) RRM, $s = 0.138$.

Figure 13. Growth tracks of typical coherent turbulent vortex structures present in the low-density ratio simulations. The solid line represents the mean visual thickness of the mixing layer.

along the structures. The nature of the imposed inflow condition has no significant bearing on the mean structure convection velocity.

Topographical features of a turbulent vortex structure can be analysed by considering the structure in a Lagrangian frame. A structure is reduced to rest in the Lagrangian frame through the vector field $(\tilde{u}_z - U_c, \tilde{v}_z)$, where $\tilde{v}_z$ is the spanwise averaged vertical velocity. The Lagrangian streamlines of the typical vortex structure are shown in figure 12(c). There is an obvious centre of rotation at $x/\theta_i = 910$, which is vertically aligned with the local accelerations in the freestreams (figure 12(a)). In addition, two saddle points are present; one upstream of the centre of rotation, and one downstream of it. The saddle points define the streamwise length of the structure.

The mean structure spacing, l, in each simulation is calculated by two distinct methods. Firstly a frequency analysis is performed on the velocity traces (such as that shown in figure 12(b)) recorded at three streamwise locations, namely $x/\theta_i =$ 626, 1000, and 1314. As the structures convect at a constant speed, the spacing of the structures can easily be determined from the dominant structure passage frequency. Secondly the distance between the bounding saddle points of each structure is computed over the lifetime of the structure, and a mean value is obtained. The mean spacing values obtained from these two methods are closely matched, with the average from the two methods presented in table 2. The values are normalised by the streamwise distance from the virtual origin. For a given density ratio, the mean spacing is similar for the RRM-type and WN-type simulations. Of particular note is that the structure spacing is a function of the density ratio — increasing the value of s leads to an increase in the normalised structure spacing.

Finally, the growth of the turbulent vortex structures is analysed. In order to calculate the structure diameter, a vertical line is drawn through its centre of rotation, and the vertical positions where this line intersects the $\zeta_z = 0.01$, 0.99 contours is stored. The diameter of the structure is the vertical distance between these two points. This method has been used to record structure evolution in previous numerical simulations (McMullan *et al* 2015, McMullan and Garrett 2016a), and experimental studies (D'Ovidio and Coats 2013). Tracks of representative structures from the $s = 0.138$ simulations are shown in figure 13. The solid line in each image is the mean visual thickness of the mixing layer. In the WN-type simulations the structures grow continuously and linearly as they convect downstream. The overall self-similar growth of the mixing layer is determined by the linear growth of the diameter of each structure. Interactions between the structures serve to reduce the number density of the structures, and contribute nothing to the overall growth of the layer (McMullan *et al* 2015). The merging-type, and tearing-type interactions that occur between continuously and linearly growing structures have been documented elsewhere (McMullan and Garrett 2016a). The continuous and linear growth of turbulence vortex structures has been observed in numerical simulations of the uniform density mixing layer (McMullan *et al* 2015), and in experiments of the variable-density mixing layer (D'Ovidio and Coats 2013). It is important to note, however, that the mixing layers reported in the experimental study originated from initial conditions that would not typically be described as 'clean' (D'Ovidio 1998).

In the RRM-type simulation, an entirely different pattern of turbulent vortex structure growth is observed. The structures grow rapidly following their birth, but this growth tails off as the structures reach the end of their lives. Whilst the structure growth is continuous throughout the structure lifetime, it follows a square-root-of-time dependency. This root-time dependency is associated with continuous growth through either irrotational roll-up (Jimenez 1980), or turbulent diffusion (Moore and Saffman 1975). In order to facilitate the mean self-similar growth of the mixing layer, interactions between the structures are essential. The interactions that occur between structures in the RRM simulations are of the pairing-type, and tearing-type, which have been observed in both experiments that originate from clean initial conditions (Hernan and Jimenez 1982), and in numerical simulations (McMullan and Garrett 2016a).

5.2.2. Streamwise structure. The plan view visualisations of figures 10 and 11 show that the nature of the streamwise structure in the simulated mixing layer depends on the imposed inflow condition. The streamwise vortex structure is analysed by inspection of y–z cross planes at various streamwise locations. The mean streamwise vorticity is computed from $\Omega_x = \partial\overline{W}/\partial y - \partial\overline{V}/\partial z$, where $\overline{V}$ and $\overline{W}$ are the mean vertical and spanwise velocities respectively. Cross-plane measurements are recorded at $x/\theta_i = 0$, 43, 109, 218, 328, 656, 1000, and 1312.

Normalised mean streamwise vorticity maps at $x/\theta_i = 0$ are shown in figure 14 for the variable-density simulations. This measurement station is placed at the trailing edge of the splitter plate, and hence any streamwise vorticity present in the cross-plane maps will have been produced by the inflow condition modelling. In the WN-type calculations the cross-plane maps are devoid of any streamwise vorticity at the inflow plane. This is because the inflow disturbances in these calculations are produced by pseudo-random white noise, and are therefore spatially- and temporally-uncorrelated. These fluctuations are quickly damped out by the solution method, removing the potential for residual streamwise vorticity to form in the inflow condition. For the RRM-type simulations there are low-magnitude counter-rotating streamwise vortices embedded within the laminar boundary layers. Streamwise vortices have

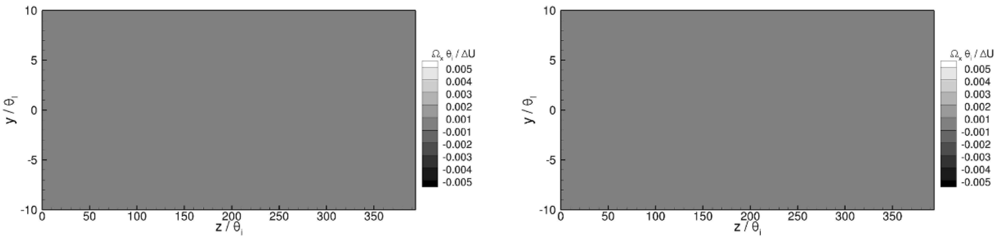

(a) WN, $s = 7.23$. (b) WN, $s = 0.138$.

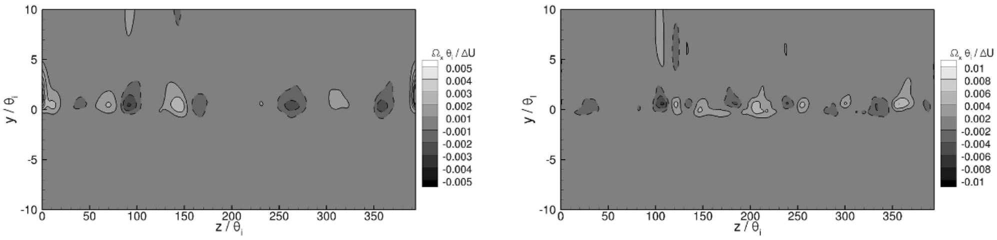

(c) RRM, $s = 7.23$. (d) RRM, $s = 0.138$.

Figure 14. Cross-plane maps of mean streamwise vorticity at the trailing edge of the splitter plate, $x/\theta_i = 0$. Note the changes in contour levels between images.

been indirectly measured through the skin friction distribution of the laminar boundary layer at the trailing edge of the splitter plate in experiments (Bell and Mehta 1992), which demonstrates that residual vortex structure is present in what are normally considered as clean laminar inflow conditions.

The normalised streamwise vorticity maps at $x/\theta_i = 109$ are shown in figure 15 for the variable-density simulations. In the WN-type case at high density ratio the flow is still devoid of streamwise vorticity. In the low-density ratio simulation of the same inflow condition type, the mean streamwise vorticity field is essentially random. In the RRM-type cases, both flows contain three-tiered clusters of mean streamwise vorticity. A central vortex is flanked by two streamwise vortices of opposite sign, and the clusters are spaced at regular intervals across the span. Inspection of the clusters shows that the signs of the vortices are reversed between neighbouring clusters. The clusters occupy the entire visual thickness of the mixing layer, with the flanking vortices extending into the freestreams. This pattern of clustering in the initial region of the mixing layer is entirely consistent with experimental observations (Bell and Mehta 1992, Wiecek and Mehta 1998). Inspection of figures 14(c), (d) and 15(c), (d) show that the streamwise vortices present in the upstream flow act as anchor points for the subsequent development of streamwise vortices in the mixing layer — a feature noted in experimental studies of streamwise vortices in shear flows (Jimenez 1983, Bernal and Roshko 1986). It is important to note that the residual streamwise vorticity present in the generated inflow condition of the RRM-type calculations is not a numerical artefact. Repeating the simulation with a different initial random field in the recycling domain leads to the vortices appearing at different spanwise locations in the upstream boundary layers—the streamwise vortex structures present in the mixing layer consequently appear at different spanwise locations, but their evolution, and mean statistical information, remain unchanged when compared to the data presented above.

Normalised mean streamwise vorticity maps at $x/\theta_i = 328$ are shown in figure 16. At this streamwise position the flow has become turbulent, as evidenced by $-5/3$ roll-off in the PSD plots in figure 9(b). In the WN-type inflow simulations there is a random distribution of mean

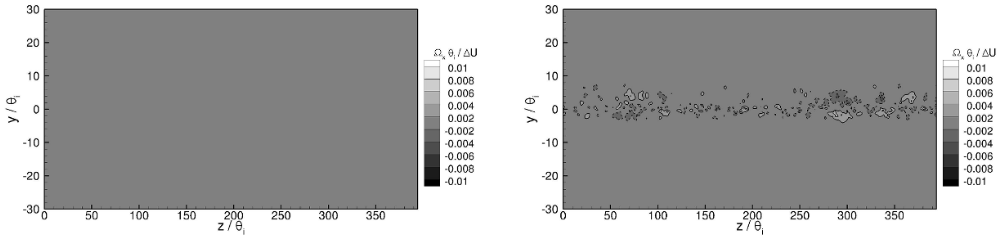

(a) WN, $s = 7.23$.

(b) WN, $s = 0.138$.

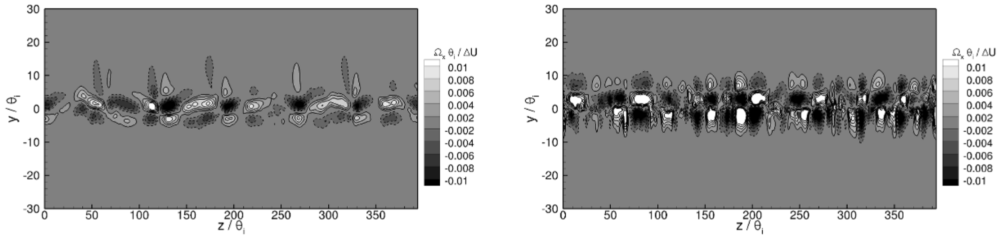

(c) RRM, $s = 7.23$.

(d) RRM, $s = 0.138$.

Figure 15. Mean streamwise vorticity maps recorded at $x/\theta_i = 109$. Vorticity normalised through the initial momentum thickness, θ_i, and the velocity difference across the layer, ΔU. Note the changes in vertical axis extent between the images.

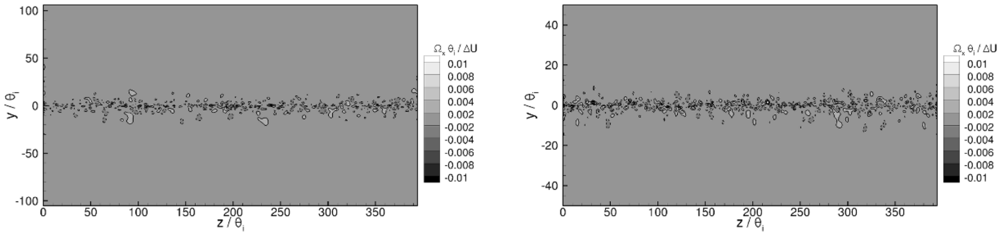

(a) WN, $s = 7.23$.

(b) WN, $s = 0.138$.

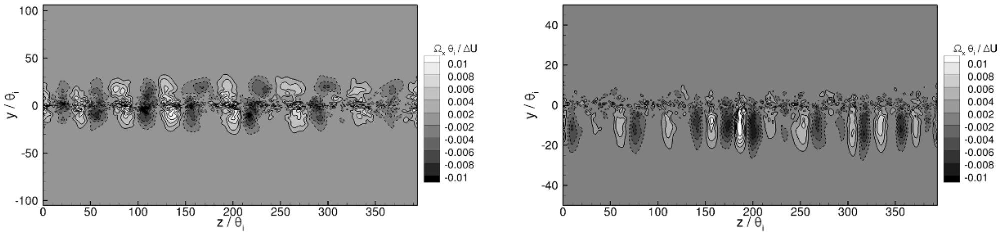

(c) RRM, $s = 7.23$.

(d) RRM, $s = 0.138$.

Figure 16. Mean streamwise vorticity maps recorded at $x/\theta_i = 328$. Vorticity normalised through the initial momentum thickness, θ_i, and the velocity difference across the layer, ΔU. Note the changes in vertical axis extent between the images.

streamwise vorticity in the cross-plane maps, as shown in figures 16(a) and (b) for $s = 7.23$, and $s = 0.138$ respectively. In contrast, the cross-plane maps from the RRM-type simulations show clear bands of alternating sign streamwise vorticity along the span of the mixing layer.

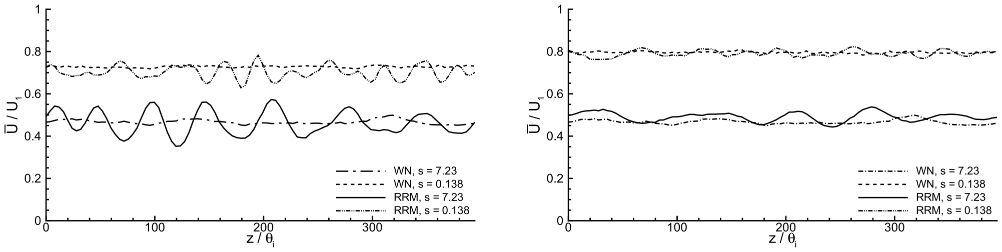

(a) $x/\theta_i = 328$.

(b) $x/\theta_i = 656$.

Figure 17. Variation of mean streamwise velocity along the span of the mixing layer. Measurements taken along the geometric plane of the splitter plate, $y/\theta_i = 0$.

The three-tiered clusters of streamwise vorticity that were present in the flow at $x/\theta_i = 109$ have realigned into a single row of alternating sign streamwise vortices. The number of vortices per unit span at $x/\theta_i = 328$ has decreased substantially from that at $x/\theta_i = 109$, which demonstrates that the realignment process has involved the pairing of like-signed vortices (Bell and Mehta 1992). The banding of the mean streamwise vorticity in the $y-z$ cross-planes is direct evidence of a streamwise structure that is statistically stationary in the variable-density, RRM-type simulations. These findings agree with the uniform-density mixing layer simulation data of McMullan and Garrett (2016a).

The spatially stationary streamwise vortex structure has a pronounced influence on the mean velocity field. An example of this is shown in figure 17, where the mean streamwise velocity across the span of the flow in the plane of the splitter plate ($y/\theta_i = 0$) is plotted at $x/\theta_i = 328$, and $x/\theta_i = 656$. There are clear peaks and valleys in the profiles obtained from the RRM-type simulations. At a given streamwise measurement location the number of peaks and valleys present in the profile is a function of the density ratio, as there are more peaks and valleys present in the $s = 0.138$ case than in the $s = 7.23$ case. These peaks and valleys are indicative of the mixing layer being wrinkled by the presence of the streamwise vortex structure. Inspection of the centreline of the $s = 7.23$ case in figure 17(a) along with the corresponding mean streamwise vorticity map (figure 16(c)) shows that the peaks and valleys in the centreline plot coincide with the interfaces between neighbouring streamwise vortex pairs; a peak occurs when the vortices have a common upflow direction, and troughs occur where the streamwise vortices have a common downflow direction. The same pattern is also observed in the $s = 0.138$ when comparing figures 16(d) and 17(a). The centreline profiles obtained at $x/\theta_i = 656$ are shown in figure 17(b). The amplitude of the peaks and valleys has reduced in the profiles from the RRM-type simulations, implying that the strength of the streamwise vortices has reduced. The distance between the peaks and valleys has widened, signifying that the spacing of the structures has increased. The profiles obtained from the WN-type calculations remain largely flat along the span at all streamwise locations, owing to the absence of an organised streamwise structure in these cases.

The wrinkling of the mixing layer by the stationary streamwise structure is also apparent in the turbulent stresses. Figures 18(a) and (b) show the primary Reynolds stress, $\overline{u'v'}$, and secondary shear stress, $\overline{u'w'}$, cross-plane maps at $x/\theta_1 = 328$ for the WN-type simulation, with $s = 7.23$. The primary Reynolds stress map is largely invariant along the span and the magnitude of the secondary shear stress is negligible when compared to $\overline{u'v'}$ as would be expected for a mixing layer lacking an organised streamwise structure (Bell and Mehta 1992). The cross-plane maps of $\overline{u'v'}$ and $\overline{u'w'}$ from the $s = 7.23$, RRM-type simulation are shown in figures 18(c)

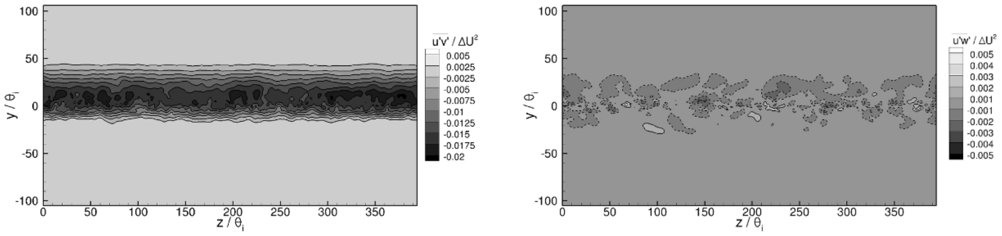

(a) WN, primary shear stress.

(b) WN, secondary shear stress.

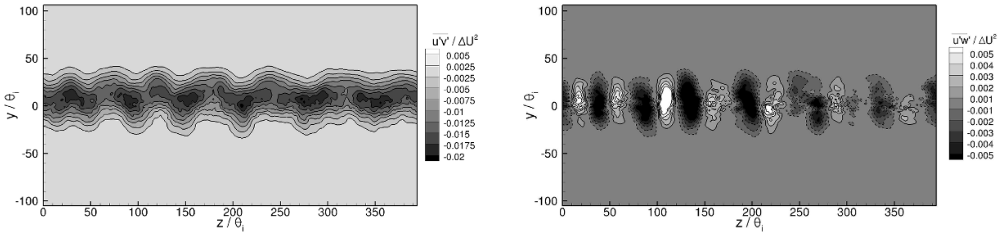

(c) RRM, primary shear stress.

(d) RRM, secondary shear stress.

Figure 18. Cross-plane Reynolds stress contour maps obtained at $x/\theta_i = 328$ in the $s = 7.23$ calculations .

and (d). The primary Reynolds stress is substantially wrinkled by the presence of the streamwise structure, and local peaks are present in the stress map. When viewed in conjunction with the mean streamwise vorticity map of figure 16(c) the winking of $\overline{u'v'}$ coincides with the locations of the streamwise vortices. The local maxima in the magnitude of the stress corresponds to the interface between neighbouring vortices, and the local minima coincide with the cores of the vortices. The secondary shear stress map in figure 18(d) shows that a single row of alternating sign bands of $\overline{u'w'}$ along the span. These bands coincide with the streamwise vortices present in figure 16(c), with signs reversed. The influence of the streamwise vortex structure on the Reynolds stresses in the variable-density mixing layer are entirely consistent with experimental observations of the uniform density flow (Bell and Mehta 1992, Wiecek and Mehta 1998), and with results obtained for the simulated mixing layer at uniform-density conditions (McMullan and Garrett 2016b).

The evolution of the streamwise vortex structure in the RRM-type simulations is evaluated by determining the mean streamwise vortex spacing at seven streamwise measurement stations, namely $x/\theta_i = 43$, 109, 218, 328, 656, 1000, and 1312. At each location the number of streamwise vortices on the mean streamwise vorticity contour map are counted directly. This value is cross-referenced against the corresponding $\overline{u'w'}$ map to ensure consistency in the measurement. Finally the number of peaks and valleys in the centreline mean streamwise velocity profile are counted and compared to the above two values. An average value of the vortex structure spacing is then computed. The evolution of the streamwise structure spacing, s_v, with streamwise distance is shown in figure 19(a). The initial reduction in the spacing is linked to the unwrapping of the three-tiered clusters of streamwise vorticity into a single row of alternating sign streamwise vortices (Bell and Mehta 1992). Following the establishment of a single row of streamwise vortices in the flow, their spacing progressively increases with increasing streamwise distance. Neither the axis nor the ordinate of figure 19(a) account for the density ratio of the flow, hence the effect of density ratio on the streamwise structure evolution

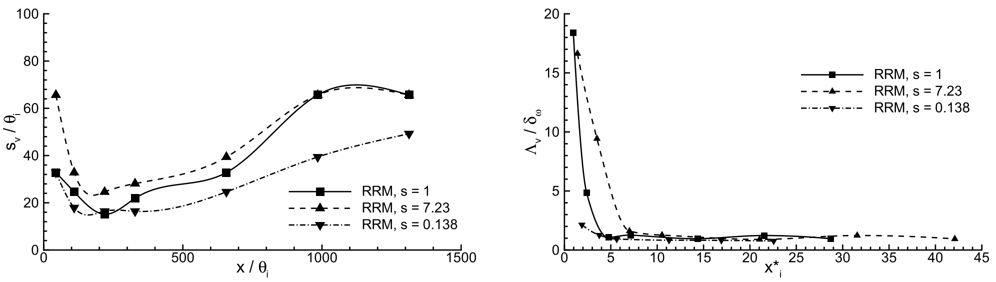

(a) Streamwise structure spacing.

(b) Ratio of streamwise structure wavelength to local vorticity thickness.

Figure 19. Statistical information on the spacing of the streamwise vortices present in the RRM-type simulations. Streamwise distance in (b) is normalised into the pairing parameter, x_i^* to accommodate for differences in flow evolution caused by the effect of the density ratio.

is not clear. We instead consider the spanwise wavelength of the streamwise structure, Λ_v, which is twice the mean structure spacing, $\Lambda_v = 2s_v$. To account for the dependency of the spatial growth rate on the density ratio, the streamwise structure wavelength is normalised by the local local vorticity thickness, $\delta_\omega = (U_1 - U_2)/\partial\overline{U}/\partial y|_{\max}$. The streamwise co-ordinate is normalised into the pairing parameter, defined as

$$x_i^* = \frac{0.017(U_1 - U_2)x}{U_c\theta_i} \tag{17}$$

for a variable-density mixing layer (D'Ovidio and Coats 2013). The normalised evolution of the streamwise structure wavelength with the pairing parameter is shown in figure 19(b). Once density ratio effects are factored in to the data, it becomes clear that the ratio of streamwise structure wavelength to local vorticity thickness approaches one for all values of the density ratio considered here. To a first-order estimate, therefore, Λ_v/δ_ω asymptotes towards a value of unity, independent of the density ratio. The asymptotic value of $\Lambda_v/\delta_\omega \approx 1$ is in good agreement with experimental data; Bernal and Roshko obtained a value of $\Lambda_v/\delta_\omega = 0.8 \pm 0.14$ for a mixing layer with $s = 7.23$, $R = 0.45$ (Bernal and Roshko 1986), Bell and Mehta obtained $\Lambda_v/\delta_\omega = 1.28 \pm 0.21$ for a uniform density flow at $R = 0.25$. Bell and Mehta (1992), and Jimenez obtained $\Lambda_v/\delta_\omega \approx 1 - 1.25$ (Jimenez 1983), also for a flow of uniform density at $R = 1$.

It is clear that the RRM-type simulations capture flow features that are essential to accurately replicate the laboratory mixing layer. In the real flow, it is known that the streamwise vortex structure in the mixing layer originates from residual streamwise vorticity in the upstream laminar boundary layers (Bell and Mehta 1992). The upstream disturbances are produced by defects in the smoothing screens (Bernal and Roshko 1986), nicks in the splitter plate (Jimenez 1980), or other geometric features in the wind tunnel (Plesniak *et al* 1993). The WN-type simulations fail to replicate these features because the residual streamwise vorticity is not generated by the pseudo-random white noise disturbances. In contrast, these features are present in the RRM-type calculations because the inflow generation technique can replicate the structure found in the upstream conditions. The results presented here are in excellent agreement with previous uniform-density mixing layer simulations which incorporated an inflow generation technique (McMullan and Garrett 2016a), and they demonstrate that the streamwise structure can be successfully generated for the variable-density flow.

6. Conclusions

In this paper we have used LES to simulate the variable density mixing layer at high Reynolds number. The goal of the research was to capture the large-scale streamwise-orientated, and spanwise-orientated structures that exist in the mixing layer which originates from clean laminar upstream conditions. An idealised inflow condition, based on a mean streamwise velocity profile perturbed with Gaussian white noise, produces a mixing layer which contains large-scale spanwise structures, but does not capture the spatially stationary streamwise structure, at any density ratio. This deficiency is caused by an absence of low-level streamwise vorticity in the inflow condition. An inflow condition produced by an inflow generator produces a correlated flow-field that is fed into the mixing layer simulation, and residual streamwise vorticity is present in the inflow data. This residual streamwise vorticity generates three-tiered clusters of streamwise vortices in the initial region of the mixing layer, which realign into a single row of alternating sign streamwise vortices. The streamwise vortices evolve such that the ratio of structure wavelength to local vorticity thickness attains a value of unity for all density ratios. It is not yet clear if this scaling is independent of both the density ratio and the velocity ratio. The large-scale spanwise structures in both simulation types having spacings that are a function of the density ratio — this finding indicates that further research is required to improve growth and entrainment models to account for this dependency.

This research adds to the body of evidence concerning the simulation of the initially-laminar mixing layer found in experimental apparatus. It is clear that the idealised inflow condition produces mixing layers which lack important features that appear in the real flow. Given that the WN-type mixing layers produce mixing layers that have a unique self-similar state, this type of inflow condition should be used for simulations where new numerical methods are to be validated. The absence of key flow physics in these simulations render them appropriate for qualitative comparison only, when studying the laboratory mixing layer. If quantitative comparisons are to be drawn against the real laboratory mixing layer, efforts must be made to accurately replicate the flow conditions found at the trailing edge of the splitter plate in the experiment. Unfortunately, almost all published experiments of the mixing layer have initial conditions which are not adequately documented for direct replication by numerical simulation, hence further experiments are required to produce a complete initial condition dataset on which numerical simulations can be based.

Acknowledgments

This research was performed on ALICE2, the University of Leicester High Performance Computing Service. The authors would like to thank C M Coats for many constructive discussions in the early stages of this work.

References

Almagro A, García-Villalba M and Flores O 2017 *J. Fluid Mech.* **830** 569–601
Attili A and Bisetti F 2012 *Phys. Fluids* **24** 035109
Balaras E, Piomelli U and Wallace J M 2001 *J. Fluid Mech.* **446** 1–24
Baltzer J R and Livescu D 2020 Modeling and Simulation of Turbulent Mixing and Reaction. Heat and Mass Transfer (Singapore: Springer) pp 1–23
Bell J H and Mehta R D 1990 *AIAA J.* **28** 2034–42
Bell J H and Mehta R D 1992 *J. Fluid Mech.* **239** 213–48

Bernal L P and Roshko A 1986 *J. Fluid Mech.* **170** 499–525
Browand F K and Latigo B O 1979 *Phys. Fluids* **22** 1011–9
Browand F K and Troutt T R 1980 *J. Fluid Mech.* **97** 771–81
Browand F K and Troutt T R 1985 *J. Fluid Mech.* **158** 489–509
Brown G L and Roshko A 1974 *J. Fluid Mech.* **64** 775–816
Brown G L and Roshko A 2012 *J. Turbul.* **13** N51
Chandrsuda C, Mehta R D, Weir A D and Bradshaw P 1978 *J. Fluid Mech.* **85** 693–704
Comte P, Lesieur M and Lamballais E 1992 *Phys. Fluids A: Fluid Dyn.* **4** 2761–78
Comte P, Silvestrini J and Bégou P 1998 *Eur. J. Mech.* **17** 615–37
D'Ovidio A 1998 Coherent structures in turbulent mixing layers *PhD Thesis* University of Leicester
D'Ovidio A and Coats C M 2013 *J. Fluid Mech.* **737** 466–98
Dianat M, Yang Z, Jiang D and McGuirk J J 2006 *Flow Turbul. Combust.* **77** 205–27
Dimotakis P E 1986 *AIAA J.* **24** 1791–6
Dimotakis P E 2000 *J. Fluid Mech.* **409** 69–98
Dimotakis P E and Brown G L 1976 *J. Fluid Mech.* **78** 535–60
Dziomba B and Fiedler H E 1985 *J. Fluid Mech.* **152** 419–42
Hermanson J C and Dimotakis P E 1989 *J. Fluid Mech.* **199** 333–75
Hernan M A and Jimenez J 1982 *J. Fluid Mech.* **119** 323–45
Huang J X, Hug S N and McMullan W A 2017 *Numerical Methodologies for DNS and LES* AIAA 2017-3295
Huang L S and Ho C M 1990 *J. Fluid Mech.* **210** 475–500
Jimenez J 1980 *J. Fluid Mech.* **96** 447–60
Jimenez J 1983 *J. Fluid Mech.* **132** 319–36
Karasso P S and Mungal M G 1996 *J. Fluid Mech.* **323** 23–63
Konrad J H 1976 An experimental investigation of mixing in two-dimensional turbulent shear flows with applications to diffusion-limited chemical reactions *PhD Thesis* (Caltech)
Koochesfahani M M and Dimotakis P E 1986 *J. Fluid Mech.* **170** 83–112
Lund T S, Wu X and Squires K D 1998 *J. Comput. Phys.* **140** 233–58
McMullan W A 2015 *Int. J. Comput. Fluid Dyn.* **29** 333–45
McMullan W A 2017 *Int. J. Heat Fluid Flow* **68** 87–101
McMullan W A 2018a *Eur. J. Mech.* **67** 385–96
McMullan W A 2018b *Eur. J. Mech.* **67** 385–96
McMullan W A, Coats C M and Gao S 2011 AIAA 2011–3424 (https://doi.org/10.2514/6.2011-3424)
McMullan W A, Gao S and Coats C M 2007 *Int. J. Numer. Methods Fluids* **55** 589–610
McMullan W A, Gao S and Coats C M 2015 *J. Fluid Mech.* **762** 302–43
McMullan W A and Garrett S J 2016a *Phys. Fluids* **28** 015111
McMullan W A and Garrett S J 2016b *Int. J. Heat Fluid Flow* **59** 20–32
Meyer T R, Dutton J C and Lucht R P 2006 *J. Fluid Mech.* **558** 179–205
Monkewitz P A and Huerre P 1982 *Phys. Fluids* **25** 1137–43
Moore D W and Saffman P G 1975 *J. Fluid Mech.* **69** 465–73
Mungal M G and Dimotakis P E 1984 *J. Fluid Mech.* **148** 349–82
Nicoud F and Ducros F 1999 *Flow Turbul. Combust.* **62** 183–200
Papamoschou D and Roshko A 1988 *J. Fluid Mech.* **197** 453–77
Pickett L M and Ghandhi J B 2002 *Phys. Fluids* **14** 985–8
Plesniak M W, Bell J H and Mehta R 1993 *Exp. Fluids* **14** 286–8
Quirk J J 1997 Upwind and High-Resolution Schemes (Berlin: Springer) pp 550–69
Rogers M M and Moser R D 1994 *Phys. Fluids* **6** 903–23
Slessor M D, Bond C L and Dimotakis P E 1998 *J. Fluid Mech.* **376** 115–38
Smagorinsky J 1963 *Mon. Weather Rev.* **91** 99–164
Soteriou M C and Ghoniem A F 1995 *Phys. Fluids* **7** 2036–51
Van Driest E R 1956 *J. Aeronaut. Sci.* **23** 1007–11
Wiecek K C and Mehta R D 1998 *Exp. Therm. Fluid Sci.* **16** 165–76
Winant C D and Browand F K 1974 *J. Fluid Mech.* **63** 237–55
Xiao F, Dianat M and McGuirk J J 2017 *Flow Turbul. Combust.* **98** 663–95